Microfluid Nanofluid (2015) 19:635–646
DOI 10.1007/s10404-015-1589-x

RESEARCH PAPER

Measurement of the oscillatory flow field inside tapered cylindrical inkjet nozzles using micro-particle image velocimetry

E. Cheng[1] · A. Ahmadi[1] · K. C. Cheung[1]

Received: 4 November 2014 / Accepted: 23 April 2015 / Published online: 5 May 2015

Abstract The flow field within a tapered, cylindrical, piezoelectrically actuated glass inkjet nozzle is captured using fluorescence micro-PIV (μPIV) assisted by a novel, custom-designed PDMS micro-fabricated nozzle holder and a microsecond-resolution cyclic triggering system. The presented work overcomes key imaging challenges such as distortion from the refractive index mismatched curved glass–air interface and the typically large depth of field/correlation found in inkjet imaging set-ups. The PDMS holder permits fluorescence imaging of the seeded flow tracing particles with minimal distortion as the holder is refractive-index-matched with the glass nozzle. The cyclic triggering system allows visualization of the transient phases of a periodic droplet ejection event. The system utilizes an inverted microscope with an objective lens capable of producing a low depth of correlation of 12.25 μm. Double-frame images for μPIV were acquired beginning from the onset of droplet formation to study the flow field evolution during droplet formation and after droplet break-off. An oscillatory flow field was observed within the nozzle during the droplet ejection process which closely correlates with modelling results.

Keywords Inkjet · Micro-particle image velocimetry · Oscillatory flow field · Hydrodynamics

✉ E. Cheng
ericc@ece.ubc.ca

[1] University of British Columbia, 4060-2332 Main Mall, Vancouver, BC V6T 1Z4, Canada

1 Introduction

Drop-on-demand (DOD) inkjet printing provides a convenient method of material deposition because it can provide high droplet throughput rates, tunable ejected volumes and non-contact material deposition and is easily integrated with computer-aided design environments (Derby 2010). Due to its many advantages, DOD inkjet printing has emerged in industrial applications ranging from 3D rapid prototyping (Sachs et al. 1992), printed electronics (Sirringhaus et al. 2000; Mei et al. 2005) and life science technologies (Nakamura et al. 2005). Among numerous actuators, piezoelectric printheads are most commonly used in research as they generate droplets through deformation of the element causing a pressure wave to propagate through the inkjet nozzle. This distinct droplet formation mechanism is compatible with a wider range in the rheology of the printed inks (Yang et al. 1997; Schoeppler 2006; Fakhfouri et al. 2009; Magdassi 2009) when compared to other droplet generation systems such as thermal inkjet printheads. As a result, piezoelectric DOD inkjet printers have been used for printing colloidal suspensions in numerous life science applications including proteomics, DNA sequencing, therapeutics and tissue engineering (Chee et al. 1996; Lemmo et al. 1998; Cooley et al. 2001; Boland et al. 2006; Chahal et al. 2012; Lorber et al. 2014; Xu et al. 2014). Understanding the hydrodynamics of suspension flow inside the inkjet nozzle is an essential step in the optimization of these printheads.

In recent years, numerous modelling and experimental studies have focused on investigating the hydrodynamics of fluid flow within inkjet nozzles. Several groups have modelled the pressure and velocity field development throughout the actuation cycle and showed a damped oscillatory pressure and velocity field (Shin et al. 2005;

Suh and Son 2009). To obtain an accurate understanding of the hydrodynamics of inkjet printing, it is crucial to capture this oscillatory velocity field which has been shown to occur over very small timescales (Wijshoff 2004, 2006; Yu et al. 2007). One of the main challenges in developing numerical models for inkjet printheads is defining the upstream pressure boundary condition. The two most commonly used approaches include modelling the pressure wave caused by the displacement of the actuator (Dijksman 1984) or by direct measurement of the pressure upstream of the flow (Wijshoff 2010). To correlate the velocity and pressure fields, these numerical simulations often make simplifications in the boundary conditions and the governing equations to reduce the complexity of the equations which are solved. While the simplifications and assumptions are often justified, they can overlook important parameters such as the influence of the piezoelectric actuator or channel dimensions and nozzle geometry on the fluid field. Moreover, numerical simulation is costly in terms of computational time and resources.

Experimental studies, on the other hand, allow direct measurement of the velocity field in the nozzle using microparticle image velocimetry (μPIV) methods. μPIV systems typically utilize volume illumination from a pulsed laser as opposed to the laser sheet used in conventional PIV (Meinhart et al. 2000). Implementation of the μPIV technique to study inkjet systems, however, is challenging mainly due to the optical aberrations induced by the curved glass of cylindrical nozzles (Parker and Merati 1996). Other work overcame the refraction mismatch in cylindrical two-phase flow through compensation of the distortion using a priori knowledge of the optical aberration in holographic particle image velocimetry (Alcock et al. 2004; Wormald and Coupland 2010). However, the technique requires two parallel planes of optical access and intensive computational times and has high sensitivity to imaging artefacts, factors which may limit its use more widely.

Fluorescent μPIV was first performed on a *planar* custom inkjet cartridge (Meinhart and Zhang 2000) to measure the instantaneous velocity across droplet actuation and the shape of the meniscus. However, the geometry of a planar inkjet cartridge differs from that of a tapered cylindrical nozzle and may result in different velocity fields during the droplet ejection process. Castrejón-Pita et al. (2012a, b) performed a hydrodynamics study by imaging the flow inside a tapered cylindrical glass inkjet nozzle, but in that work, the authors used shadowgraph images and a set-up that gave a depth of field of approximately 200 μm in an inkjet nozzle with an 80-μm-diameter orifice. Due to optical aberration from the glass curvature and radial magnification due to refractive index mismatch, the nozzle appeared approximately 50 % wider in the captured images. Thus, the PIV algorithm calculated velocities that were integrated radially through the large volume (Castrejón-Pita et al. 2012a).

In the present work, volume-illuminated fluorescent μPIV is performed on a tapered cylindrical inkjet nozzle. To address challenges arising from aberrations induced by the curved glass, a custom-designed polydimethylsiloxane (PDMS) holder is fabricated and used which permits high-resolution imaging with minimal distortion from the cylindrical geometry of the inkjet nozzle. Moreover, to ensure that the timing of the μPIV frame capture is synchronized with the inkjet droplet actuation, an external cyclic triggering system is utilized to obtain the temporal resolution needed to capture the fluid motion. As a result, the velocity field evolution within the inkjet nozzle for a low-viscosity ink before and following the droplet ejection is captured.

2 Materials and methods

2.1 Inkjet system

A MicroFab MJ-ABP-01 (MicroFab, USA) piezoelectrically actuated tapered cylindrical inkjet nozzle was used for the study. It is composed of a glass channel which is 21.7 mm in length with an inner diameter of 0.457 mm. At one end, the glass channel gradually tapers to an orifice which is 80 μm in diameter. The other end of the glass channel forms a barbed fitting that is connected to the supply channel and ink reservoir. The inkjet nozzle is actuated by an annular piezoelectric element placed at the centre of the glass channel. Actuation of the piezoelectric element is achieved by a ± 11.25 V, 60 Hz bipolar waveform generated by an arbitrary function generator (Agilent 33220A) and a 50 × amplifier (TRek Model 603) placed in series.

2.2 PDMS nozzle holder

One of the challenges for μPIV in cylindrical channels, such as the nozzle used for this study, is refraction of the excitation laser source at the curved air–glass interface, such that insufficient light would reach the seeded fluorescent particles to produce a detectable image. To facilitate fluorescence imaging for μPIV, the inkjet nozzle is fixed across the stage of an inverted microscope (Nikon Eclipse TE 2000-U) by a PDMS holder as shown in Fig. 1. The PDMS holder serves two major functions: (1) it affixes that nozzle horizontally over the objective lens of the microscope; (2) it provides a refractive index matching material of $n = 1.4$ (Cole et al. 2011) to the glass nozzle of $n = 1.5$ for imaging with minimal distortion and attenuation of the excitation beam and emitted fluorescence signal at the PDMS–glass interface. The PDMS holder effectively transforms the tapered cylindrical geometry of the nozzle to a

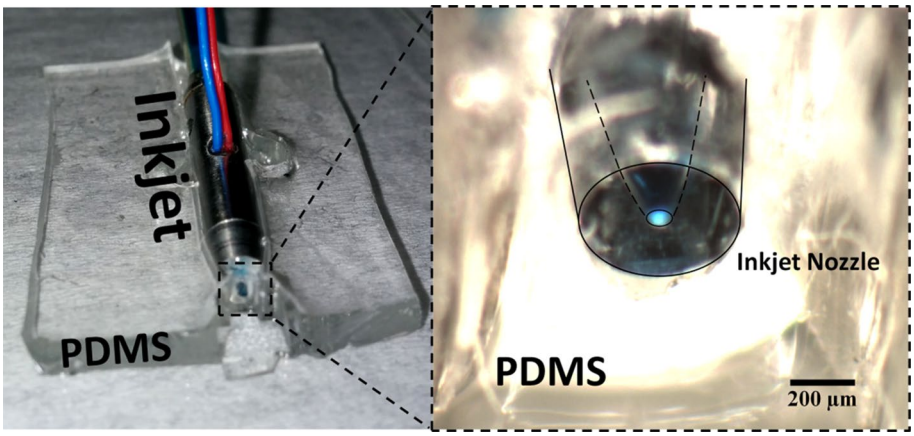

Fig. 1 Image of the inkjet nozzle in the PDMS nozzle holder. The region highlighted with the *dashed box* provides a magnified view of the inkjet nozzle within the PDMS holder acquired with a stereo microscope under 4× optical zoom. For clarity, the features of the inkjet nozzle within the PDMS are outlined

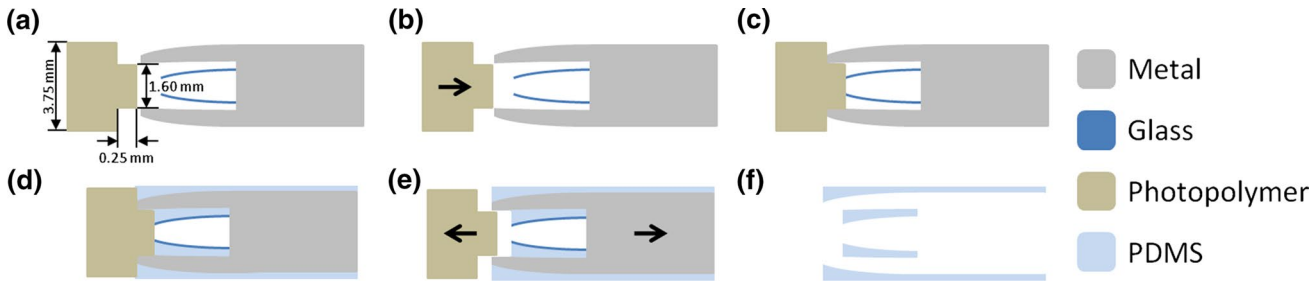

Fig. 2 Schematic of the nozzle holder fabrication process, showing the cross section across the middle plane of the inkjet nozzle. **a** An identical inkjet nozzle is fixed horizontally across a container used as a mould for the PDMS holder. **b** A 3D printed polymeric part is fitted to the front face of the nozzle orifice in order to prevent PDMS from filling the nozzle and impeding the droplet ejection process. **c** PDMS is mixed and prepared for casting. **d** PDMS is cast on the inkjet nozzle and 3D printed part. PDMS fills all open cavities including the space between the inkjet nozzle and the 3D printed part, while the inkjet nozzle cavity remains free of PDMS. The PDMS is then cured. **e** The 3D printed part is removed leaving the front face of the inkjet nozzle exposed. The inkjet nozzle is then removed. **f** The completed PDMS inkjet nozzle holder. It allows the tapered cylindrical inkjet nozzle to be encased in PDMS, giving optical access with minimal distortion while leaving the inkjet orifice free to eject droplets. The fabricated PDMS holder is then bonded onto a microscope slide

flat rectangular prism. To achieve these goals, the PDMS holder is fabricated to closely fit the inkjet nozzle with the glass nozzle, thus effectively altering the nozzle's cylindrical geometry to a rectangular prism without impeding the nozzle's function.

The nozzle holder is fabricated by casting PDMS around an identical inkjet printhead and a three-dimensional (3D) printed negative mould (Fig. 2). The 3D printed mould, composed of an opaque photopolymer (VeroWhitePlus), is designed using CAD software (SolidWorks®, Dassault Systemes) and printed by a 3D printer (Objet24, Stratasys). It is designed to fit in front of the inkjet nozzle orifice during PDMS casting in order to prevent PDMS from entering inside the nozzle mould. To fabricate the PDMS holder, an inkjet nozzle which is identical to the nozzle that will be used in the µPIV work is placed horizontally over a container. To eliminate any tilting of the inkjet nozzle within the PDMS holder, the PDMS was cast on a levelled surface. The 3D printed part is then carefully placed in contact with the orifice face of the inkjet nozzle. PDMS base and hardener are mixed in a 10:1 ratio and degassed before being cast around the nozzle and 3D printed part in the container. In order to minimize disturbance of the sensitive set-up of the inkjet nozzle and the attached negative mould, the PDMS is allowed to cure at room temperature for 6 h. Once cured, the negative mould is peeled away from the PDMS revealing a cavity and exposing the front face of the inkjet nozzle. The inkjet nozzle is then removed leaving a PDMS prism with a hollow core with the features of the glass inkjet nozzle tip. The PDMS is then bonded to a 1-mm-thick glass microscope slide using oxygen plasma to structurally reinforce the PDMS holder. Once fabricated, the PDMS fully surrounds the periphery of the glass nozzle while leaving the front face and nozzle orifice exposed, permitting unimpeded droplet formation and ejection.

2.3 µPIV imaging set-up

The flow tracing particles used for this experiment are fluorescent polystyrene particles which are 1 µm in diameter

(Thermo Scientific R0100). The particles have a peak excitation wavelength of 542 nm and a peak emission wavelength of 612 nm. The bead solution is suspended in phosphate-buffered saline at a concentration of 0.03 % w/v in preparation for printing (Adrian 1991). The viscosity of the bead solution was measured to be 0.00112 Pa s at 20.4 °C using a rheometer (Physica MCR 301, Anton Paar), and surface tension was 67.61 mN/m as measured using a tensiometer (Attension Theta, KSV Instruments). The volume fraction (φ) of our bead solution was $\varphi = 2.8 \times 10^{-4}$; it can be assumed to be a Newtonian fluid as shear-thinning behaviour was not observed for low volume fraction ($\varphi < 0.25$) suspensions of spherical particles (Mueller et al. 2010). The particle solution is supplied into the inkjet device by gravitational forces, and the back pressure in the system, as measured by a differential pressure sensor (Omega PX139) connected near the nozzle's inlet, is maintained at −500 Pa.

Volume-illuminated μPIV is achieved through an inverted microscope set-up with a Nd:YAG laser (New Wave Research Solo PIV) which is capable of producing a 5-ns pulsed laser at 532 nm for an illumination source. The average laser power per double-pulsed cycle is measured to be 350 μW (ThorLabs PM100). A schematic of the complete imaging set-up is displayed in Fig. 3. A 20× 0.35 NA super long working distance objective lens (Nikon CFI L PLAN EPI SLWD) is focused across the middle plane of the inkjet nozzle. Due to the tapered geometry of the inkjet nozzle, the middle plane was determined as the plane in which the nozzle cross section appears the widest. The depth of correlation (DOC) of the objective lens is calculated to be approximately 25 μm (Rossi et al. 2011). Double-frame images for PIV analysis are captured by a LaVision sCMOS camera which captures a two consecutive 16 bit greyscale images spaced Δt apart at 2160 × 2576 pixels with a resolution of 0.654 μm/pixel. The time between frames was acquired with a Δt of 2 or 5 μs delay depending on the expected flow velocity at each measured time point. A brightfield image of the middle plane of the inkjet nozzle acquired with the described imaging set-up shows the features of the inkjet nozzle (Fig. 4).

The timing of the PIV frame capture is synchronized with the inkjet droplet actuation by an external cyclic trigger system. At the beginning of each actuation cycle, the arbitrary function generator produces a +3.3 V TTL trigger output, the rising edge of which is received by a microcontroller (Arduino Uno) as an external hardware interrupt. The interrupt service routine on the micro-controller implements a delay (~900 μs) that allows the transient propagation of the pressure wave from the piezoelectric element to the nozzle orifice as well as a controllable microsecond resolution delay which permits imaging of the different phases of the periodic droplet ejection events. At the end of this delay, the micro-controller outputs a +5 V TTL signal to the PIV camera where the rising edge initiates a double pulse from the excitation laser spaced with Δt spacing,

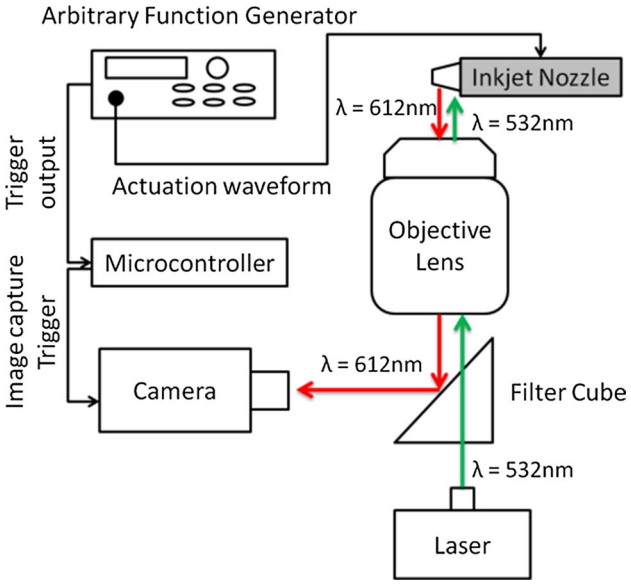

Fig. 3 Schematic of the μPIV experimental set-up. At every droplet ejection event, the arbitrary function generator produces an actuation waveform while simultaneously sending a trigger output which is received by the micro-controller. The micro-controller then implements a short delay and sends an image capture trigger which is received as a cyclic trigger by the PIV camera. Image capture is then achieved at every least common multiple between the droplet ejection frequency and the Nd: YAG laser's maximum pulsing frequency

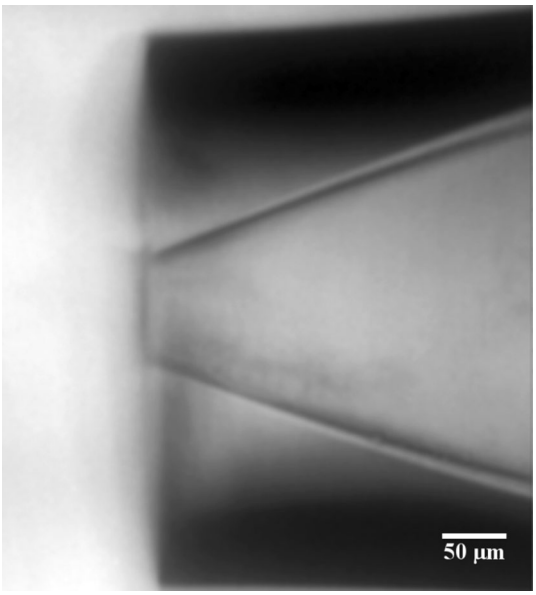

Fig. 4 Brightfield image of the inkjet nozzle, using a mercury arc lamp as the light source. In μPIV, a pulsed laser is used to acquire the image; other conditions remain the same

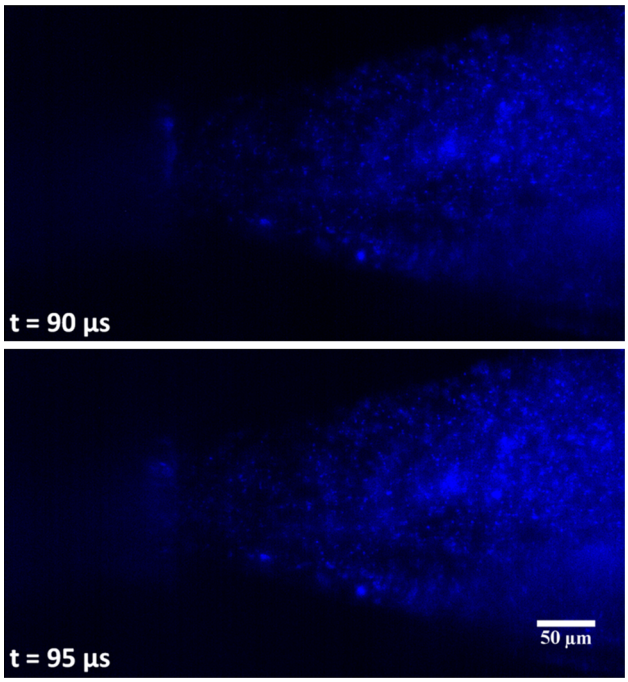

Fig. 5 A double-frame fluorescence image pair used for PIV analysis. Two consecutive images acquired in close temporal proximity permit the motion and thus velocity of the seeded particles to be measured. The camera initiated the capture of the first frame of the image pair at $t = 90$ µs, and a Δt of 5 µs was utilized to capture the second frame at $t = 95$ µs. The acquired *greyscale* image pair is *pseudo-coloured blue*. The onset of droplet formation is normalized to $t = 0$ µs as determined by the time point before fluid motion was observed

synchronized with the double-frame image capture which would be used to produce the PIV velocity vectors (Fig. 5). As the droplet ejection rate of 60 Hz is greater than the maximum double pulsing frequency of the laser excitation source of 10 Hz, the cyclic trigger initiates a phase-locked image capture at every least common multiple between the two periods, which corresponds to a PIV image at every sixth ejected droplet. By tuning the delay in the micro-controller, the triggering system permits control over the phase in which the periodic droplet ejection event is captured.

2.4 PIV analysis

Before PIV analysis, the image is preprocessed using a power filter of two by multiplying each pixel value in an image by itself. This improves the gradient between the fluorescent signals and background and has been demonstrated to decrease the DOC by a factor of two which in this case would reduce the volume integrated for PIV analysis to a thickness of only 12.5 µm (Bourdon et al. 2004). Cross-correlation for PIV analysis was performed using Davis 8 software (LaVision, Germany) with an interrogation window of 46 × 46 pixels acquired at 50 % overlap. This corresponds to a 15 µm × 15 µm interrogation window and a spatial resolution of 15 µm with velocity vectors calculated every 7.5 µm. Therefore, each velocity vector represents the average velocity within the interrogation window, vertically integrated around a 7.5-µm-thick slice across the middle plane of the inkjet nozzle. Due to the axis symmetry of the cylindrical nozzle, the observed velocity fields within the middle plane of the nozzle can be extrapolated to be representative of the entire volume by assuming radial symmetry in the velocity fields. The orientation of the PIV velocity vectors is oriented in such a way that the lateral flow is positive out of the inkjet nozzle away from the nozzle orifice.

3 Results and discussion

Through the use of a refractive index matching PDMS holder, fluorescent µPIV was performed on a cylindrical inkjet nozzle. The system utilizes an inverted microscope with the nozzle affixed horizontally above the objective lens. The long working objective lens allows for high resolution and low depth of correlation imaging of the centre plane of the inkjet nozzle. Due to the axisymmetric geometry, the 2D images are representative of the entire 3D volume of the nozzle cavity and the low DOC allows us to assume that out-of-plane particle motion is negligibly small. In this set-up, the surface tension forces dominate over the gravitational forces, allowing droplet ejection when the inkjet nozzle is placed horizontally over the inverted microscope stage (Xu and Basaran 2007): the Bond number ($\mathrm{Bo} = \rho g r^2/\sigma$), where ρ is the fluid density, g is the gravitational acceleration, r is the nozzle radius, and σ is the surface tension, in the inkjet nozzle is $\mathrm{Bo} \approx 0.0002$. Due to the density differences between polystyrene and PBS, bead sedimentation is expected to occur over time. However, the effects of sedimentation of the seeded fluorescence particles are negligible due to the small density differences and small timescales.

µPIV was performed on the first 210 µs of the droplet ejection cycle with the onset of droplet formation normalized to $t = 0$ µs as determined by the time point before fluid motion was observed. PIV double-frame images were acquired 2–5 µs apart. Using the experimental set-up, the velocity field inside the nozzle can be measured at different times. As seen in Fig. 6, the overall velocity trend agrees with previously modelled flow fields with an oscillating pressure boundary condition (Suh and Son 2009). Both modelled results from *Suh and Son* and our measured instantaneous µPIV velocity fields show that the flow was uniform in direction for each sampled time point and no recirculation flows occur. During flow reversal, the velocity

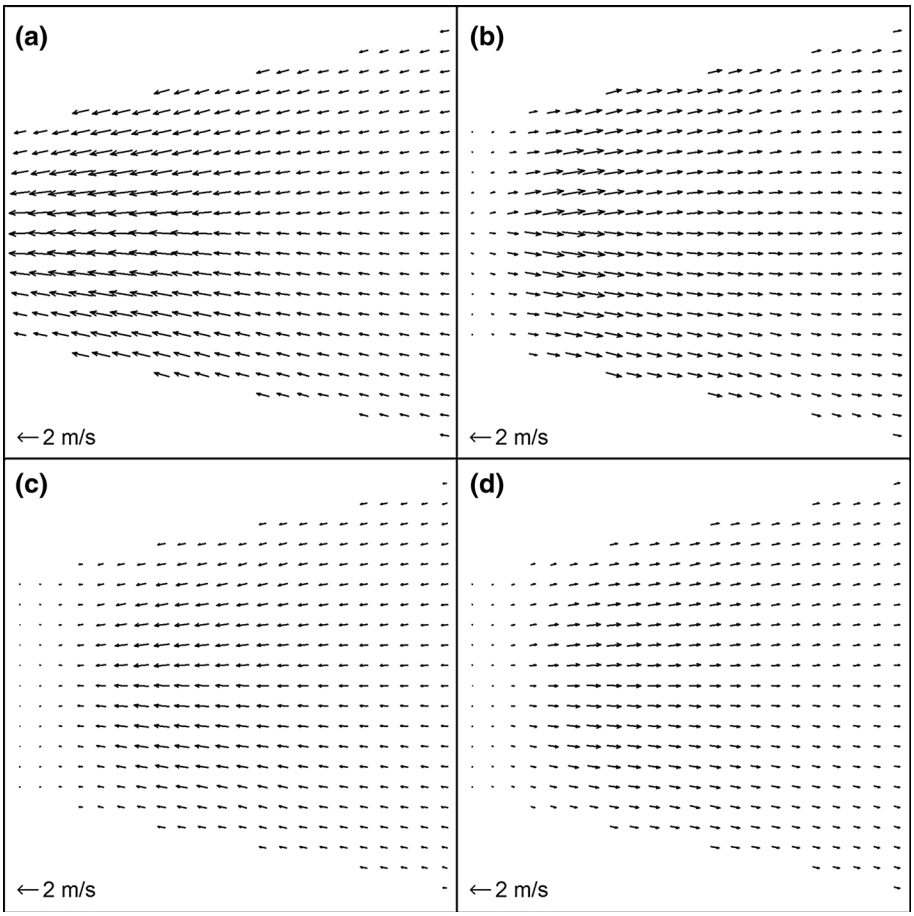

Fig. 6 PIV vectors at **a** $t = 12$ µs, **b** $t = 32$ µs, **c** $t = 50$ µs and **d** $t = 65$ µs. Reference velocity vector found on the *bottom left* corner of each velocity field represents 2 m/s

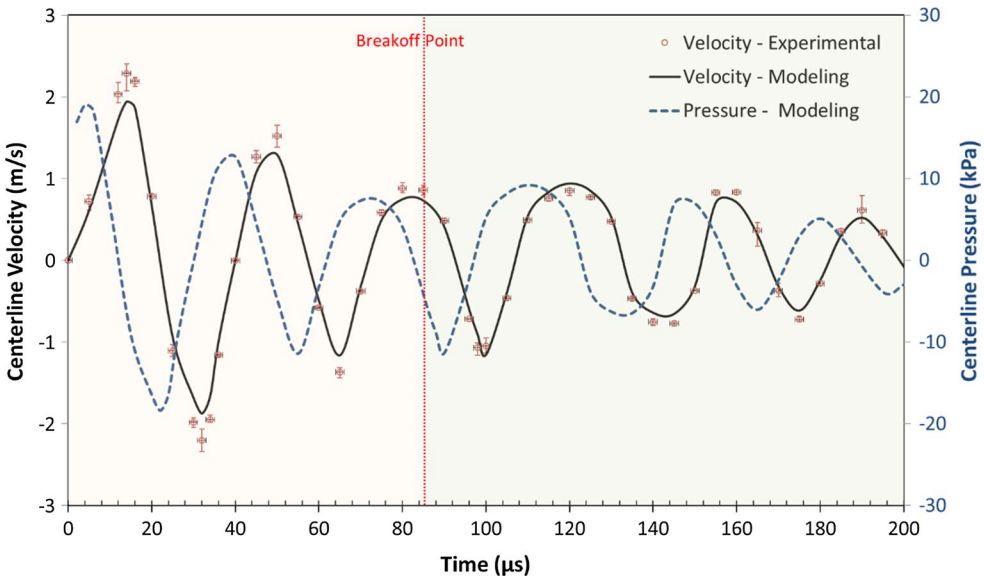

Fig. 7 Measured and calculated centreline velocity and calculated centreline pressure at 50 µm away from the nozzle orifice, averaged over three trials. The onset of droplet formation is normalized to $t = 0$ µs. The error bars represent the maximum and minimum range of velocities measured at the specific time point

fields gradually decrease in magnitude then completely reverse in direction. Along the centreline, the velocity vectors are entirely composed of the longitudinal component as radial flow along the centreline of the inkjet nozzle is zero. Away from the centreline, radial components of the velocity vector can be observed which can be attributed to the tapering in the nozzle geometry.

To get a better understanding of the changes in the velocity, the centreline axial velocity at 50 µm away from the orifice is plotted over time with each point averaged across

three identical samples as plotted in Fig. 7. For expected velocity fields greater than ± 1 m/s, a time between frame (Δt) of 2 μs was chosen; this included time points at $t = 12$, 14, 16, 32, 34, 36, 50 and 65 μs. A Δt of 2 μs permits more accurate measurement of higher velocities; as an example, a measured velocity of 2.3 m/s correlated to an average particle displacement of 15 pixels or 33.3 % of the interrogation window. All the other data points were acquired at $\Delta t = 5$ μs. At the onset of droplet formation, the velocity field was observed to be positive as the flow was directed outwards of the nozzle. A peak positive centreline velocity of 2.29 m/s was observed at $t = 14$ μs. After the peak positive centreline velocity, the velocity field gradually decreases in magnitude until flow reversal occurs between $t = 20$ and 25 μs. The flow field then reverses until a peak negative velocity of −2.20 m/s at $t = 32$ μs. The flow field continues to oscillate for another cycle reaching a secondary positive peak of 1.52 m/s at $t = 50$ μs and a secondary peak negative value of −1.37 m/s at $t = 65$ μs. After this, the droplet break-up was observed to occur at $t = 85$ μs. Before droplet break-off, the net velocity flow was positive as the peak positive velocities were greater than the peak negative velocities and the general flow direction was towards the inkjet orifice. After the droplet break-off, the flow produces a peak negative flow velocity of −1.07 m/s at $t = 98$ μs and a peak positive velocity of 0.85 m/s at $t = 120$ μs. For the first time, the peak negative velocity was greater than the subsequent peak positive velocity. This is due to the retracting meniscus which occurs after droplet break-off imparting a negative overall flow on the system.

To understand the hydrodynamics of fluid flow and investigate the relationship between the velocity and pressure fields, an analytical model (Appendix 1) was developed, and equations are solved using MATLAB® (The MathWorks). As shown in Fig. 7, the measured velocities are in good agreement with the modelling results. The observed larger difference between the modelling and experimental results around the peak values can be attributed to deviation from the unidirectional flow assumption in the model.

To further characterize the flow inside the nozzle and in particular to understand the relationship between the pressure and velocity fields, the Womersley number (Wo), which relates pulsatile flow frequency (transient inertial forces) to viscous effects, can be calculated as:

$$\mathrm{Wo} = D\left(\frac{\omega}{\nu}\right)^{1/2} \approx 35, \tag{1}$$

where D is the average diameter (100 μm), ω is the angular speed of the oscillation of the flow (150×10^{-3} s^{-1}) and ν is the kinematic viscosity (1.2×10^{-3} m^2 s^{-1}). The high value of Womersley number indicates that there is $\pi/2$ phase difference between the pressure gradient and velocity fields, and this phase delay is confirmed with modelling results (shown in Fig. 7). The calculated pressure gradient at each point in the channel is $\pi/2$ behind the local velocity. For instance, at $t = 0$, the velocity at 50 μm away from the orifice is zero, and therefore, the pressure gradient at that point has its maximum negative value. The pressure at the orifice is assumed to be atmospheric pressure, and due to the assumed positive direction towards the orifice, the pressure at 50 μm at $t = 0$ has approximately its highest positive value. An interesting behaviour of the pressure and velocity fields happens when both velocity and pressure gradient values are positive (for example during $t = 10$ and 20 μs). The positive values of the pressure gradient and the velocity during this time period mean that when the fluid moves towards the orifice, it enters a higher-pressure region and therefore experiences an additional resisting force that tends to push particles that are suspended in the fluid away from the nozzle orifice. This effect may play an important role in the motion of larger cell-sized particles (~12 μm in diameter) at the nozzle orifice, such as in the case of printing colloidal suspensions, which may be reflected backwards into the nozzle (have net negative displacement after droplet formation) as observed in previous studies (Cheng et al. 2014). The observed oscillating velocity fields are a result of the propagating actuation pressure wave as it is reflected at the boundaries of the inkjet channel. Due to the low viscosity of the ink used, the pressure wave experiences low acoustic damping. The oscillating flow fields would be mainly produced by the actuation pressure wave; however, other forces such as the capillary action of the extruded liquid would also influence the measured velocity fields within the system.

Figure 8 shows the centreline velocity for selected time points (14, 32, 50, 65 and 85 μs) across the axial direction of the inkjet nozzle. As expected, due to the tapered geometry of the nozzle, the centreline velocity decreases (in magnitude) as the distance from the nozzle orifice increases. While the PDMS holder refractive index matches that of the cylindrical glass nozzle, reducing distortion at the air–glass interface, a liquid–glass interface still remains in the system. The distortion observed from this interface is mainly in the radial direction within a tapered cylindrical geometry (Castrejón-Pita et al. 2012a, b). The distortion in the axial direction is negligible due to the linear tapering of the nozzle in the axial direction causing a constant refraction angle of the emitted fluorescence signal at the liquid–glass interface. As the velocity vectors are measured by the relative displacement of the particles between the captured double-frame images, a constant shift in the particle coordinates would not affect the magnitude of the axial velocity vectors measured. As a result, measurements along the centreline of the inkjet nozzle such as those shown in Figs. 7 and 8 are free of any optical distortion in both the position and magnitude of the velocity vectors calculated. The optical distortion in

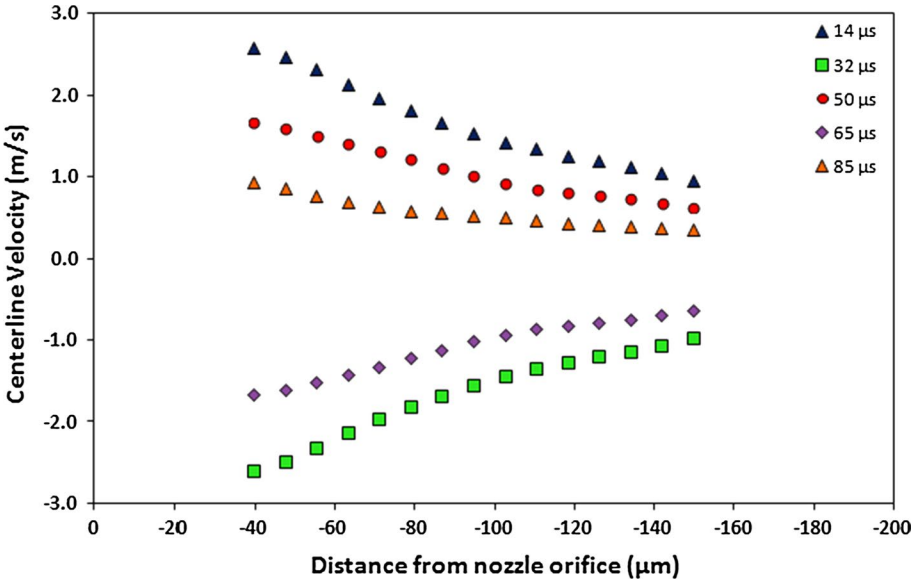

Fig. 8 Centreline velocity for selected time points (14, 32, 50, 65 and 85 µs) across the axial direction of the inkjet nozzle. The nozzle orifice is normalized to $x = 0$, with x decreasing with distance into the nozzle

the measurement in the radial direction can be theoretically calculated through ray tracing as depicted in Fig. 10 and in Eq. (2) and is in agreement with previous work (Kang et al. 2004; Minor et al. 2007). The distortion in the radial measurements is dependent on the distance of the particle away from the centre point (d) and the cross-sectional radius (R). The radial measurement error normalized with the cross-sectional radius is derived in Appendix 2.

$$\text{error} = \sqrt{R^2 - d^2} \tan\left[\sin^{-1}\left(\frac{d}{r}\right) - \sin^{-1}\left(\frac{n_1 \cdot d}{n_2 \cdot R}\right)\right] \quad (2)$$

Due to the liquid–glass interface in the inkjet nozzle, the position of the acquired velocity vectors is radially distorted. This can be easily corrected by shifting each velocity vector position (d/R) by the factor (e/R) according to Fig. 11 in Appendix 2. Although the magnitude of the radial distortion is small, this shifting was performed to correct the measured velocity values at different radial positions (as shown in Fig. 9). The observed deviation from the parabolic velocity profile and the change in the curvature of the velocity profile are attributed to the high Womersley number inside the nozzle.

The work presented here is the first direct measurement of the velocity fields within a cylindrical inkjet nozzle. The µPIV results show an oscillating velocity field within the inkjet nozzle during the droplet ejection cycle. This corresponds with previous work on numerical simulation and measurements of pressure waves within the inkjet nozzle. Wijshoff developed a system named Piezo-Acoustic sensing of INk channels in the time domain (Paint) to directly measure the pressure waves within the inkjet channel (Wijshoff 2010). The system utilized the piezoelectric element which actuates the inkjet nozzle to both produce and record the reflected pressure waves at the piezoelectric element which is placed at the centre of the inkjet channel. The measured Paint signal shows the oscillating pressure wave propagating within the inkjet channel. Additionally, numerical simulations of the flow fields predicted the occurrence of uniform flow oscillations during the droplet formation process (Suh and Son 2009).

4 Conclusion

For the first time, fluorescence µPIV was performed on a cylindrical inkjet nozzle. A refractive index matching holder reduced imaging distortion, while the objective lens gave a low depth of correlation, permitting direct measurement of the flow field. Oscillating flow fields were observed to develop during the droplet formation process as well as after droplet ejection. A peak positive velocity of 2.29 m/s and a peak negative velocity of −2.2 m/s were observed to occur before droplet break-off. The direct measurements of the oscillating flow field confirm previous work on flow field modelling and previous measurements of the pressure waves which implied an oscillatory flow. This work would help future developments in inkjet printing technologies, especially in the printing of colloidal solutions such as cell suspensions which is an increasing area of interest for research and technology development.

Acknowledgments This work is funded in part by the Natural Sciences and Engineering Research Council of Canada (NSERC).

Conflict of interest The authors declare that they have no conflict of interest.

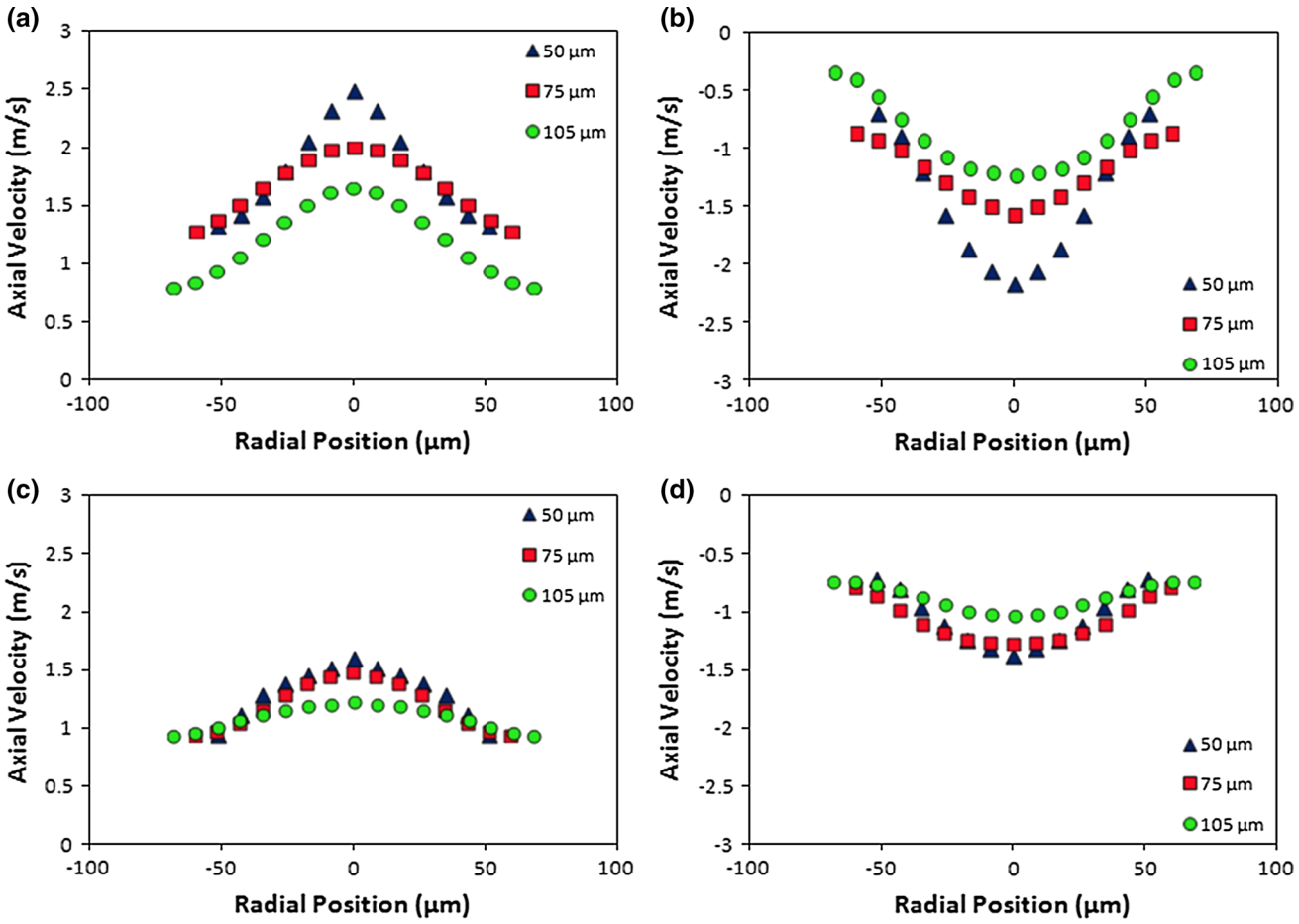

Fig. 9 Axial velocity plotted across the inkjet nozzle radial cross section at 50, 75 and 105 μm away from the nozzle orifice. The selected time points plotted were at **a** $t = 14$ μs, **b** $t = 32$ μs, **c** $t = 50$ μs and **d** $t = 65$ μs. The radial position of each velocity point plotted is corrected based on the expected degree of distortion as shown in Fig. 11 in Appendix 2. No correction to the measured velocity is necessary as the error is only found in the radial direction of the inkjet nozzle

Appendix 1

The governing equation for the fluid flow inside the tapered nozzle is the Navier–Stokes equation as:

$$\frac{\partial u_z}{\partial t} + u_r \frac{\partial u_z}{\partial r} + u_z \frac{\partial u_z}{\partial z} = -\frac{1}{\rho_f}\frac{\partial p}{\partial z} + \upsilon\left(\frac{\partial^2 u_z}{\partial r^2} + \frac{1}{r}\frac{\partial u_z}{\partial r} + \frac{\partial^2 u_z}{\partial z^2}\right), \tag{3}$$

where u_z and u_r are the z- and r-component of velocity, respectively, ρ_f is the fluid density and υ is the fluid kinetic viscosity. In this analysis, it is assumed that fluid is incompressible and the walls are rigid. Moreover, it is assumed that pressure gradient in r-direction, convective terms and $\frac{\partial^2 u_z}{\partial z^2}$ are negligible (Shin et al. 2005). Therefore, the linearized Navier–Stokes equation for unidirectional flow becomes

$$\frac{\partial u_z}{\partial t} = -\frac{1}{\rho_f}\frac{\partial p}{\partial z} + \upsilon\left(\frac{\partial^2 u_z}{\partial r^2} + \frac{1}{r}\frac{\partial u_z}{\partial r}\right) \tag{4}$$

It can be shown that the analytical solution to the linearized Navier–Stokes equation for an oscillatory pressure gradient of

$$\frac{\partial p}{\partial z} = \exp(i\omega t) \tag{5}$$

is (Shin et al. 2005)

$$u_z(r, z, t) = u(r, z)\exp(i\omega t), \tag{6}$$

and

$$u(r, z) = \frac{1}{\rho_f i\omega}\left(1 - \frac{J_0(\lambda r)}{J_0(\lambda R(z))}\right), \tag{7}$$

where

$$R(z) = R_1 - z\tan\theta \tag{8}$$

and

$$\lambda = \sqrt{-i\omega/\upsilon}. \tag{9}$$

In these equations, J_0 is the Bessel function of first kind, θ is the tapered angle and R_1 is the inner radius at the upstream of nozzle. On the other hand, the equation for pressure, $p(z)$, can be obtained from the continuity equation as:

$$\int_0^{R(z)} \frac{\partial}{\partial r}(ru_r)dr + \frac{\partial}{\partial z}\left(\int_0^{R(z)} ru_z dr\right) = 0, \tag{10}$$

which simplifies to

$$\frac{\partial^2 p(z)}{\partial z^2} + F_3(z)\frac{\partial p(z)}{\partial z} = 0, \tag{11}$$

where $F_3(z) \equiv F_2(z)/F_2(z)F_1(z).F_1(z)$, and $F_1(z)$ and $F_2(z)$ are defined as

$$F_1(z) = \int_0^{R(z)} r - \frac{J_0(\lambda r)}{J_0(\lambda R(z))}\mathrm{d}r \tag{12}$$

$$F_2(z) = \int_0^{R(z)} rJ_0(\lambda r)\mathrm{d}r \frac{\lambda \tan\theta\, J_1(\lambda R(z))}{(J_0(\lambda R(z)))^2} \tag{13}$$

As a result, the pressure and velocity fields can be obtained as:

$$p(z) = C_1 + C_2 \int_{z_1}^{z} \exp\left(-\int_{z_1}^{\zeta} F_3(\xi)\mathrm{d}\xi\right)\mathrm{d}\zeta \tag{14}$$

$$u(r,z) = -\frac{C_2}{\rho_f i\omega}\left(1 - \frac{J_0(\lambda r)}{J_0(\lambda R(z))}\right)\exp\left(-\int_{z_1}^{z} F_3(\xi)\mathrm{d}\xi\right) \tag{15}$$

Due to the linear nature of the simplified Navier–Stokes equation, in most of the previous studies (Shin et al. 2005; Shin and Smith 2008), the pressure resulting from the piezoelectric actuator is expressed as a sum of oscillating pressure using Fourier series, and the velocity field is found by superposition. However, in this study, the velocity field is measured directly. Therefore, using Fourier series, the measured velocity at the upstream of the flow (at $z = 105$ μm) can be expressed as a sum of oscillating velocity terms, and as a result, the pressure field and velocity at other points can be found.

Appendix 2

The error due to distortion from the liquid–glass interface is calculated by projecting the refracted light ray back to the imaging plane and finding the difference of the projected position relative to the original particle position (Fig. 10). This is first done with Snell's law.

$$n_1 \sin(\theta_1) = n_2 \sin(\theta_2) \tag{16}$$

$$\theta_2 = \sin^{-1}\left(\frac{n_1}{n_2}\sin(\theta_2)\right) \tag{17}$$

The angle in which the refracted light is deviated from the undistorted path (θ_d) is then identified by

$$\theta_d = \theta_1 - \theta_2 \tag{18}$$

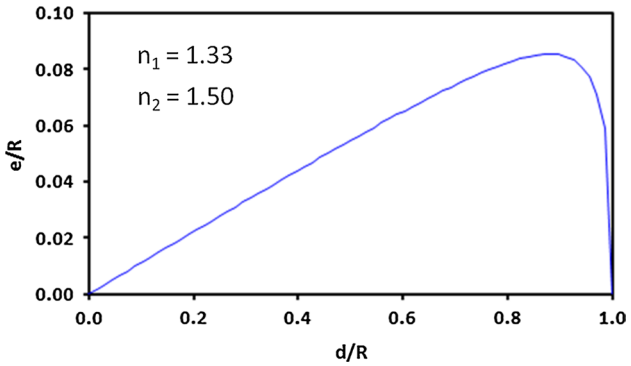

Fig. 11 The degrees of deviation in the radial direction due to the liquid–glass interface at the boundary of the inkjet nozzle as a function of the distance along the nozzle radius normalized to the cross-sectional radius of the inkjet nozzle. Due to the close refractive indices, the degree of deviation is small relative to the distortion present in a cylindrical air–glass interface

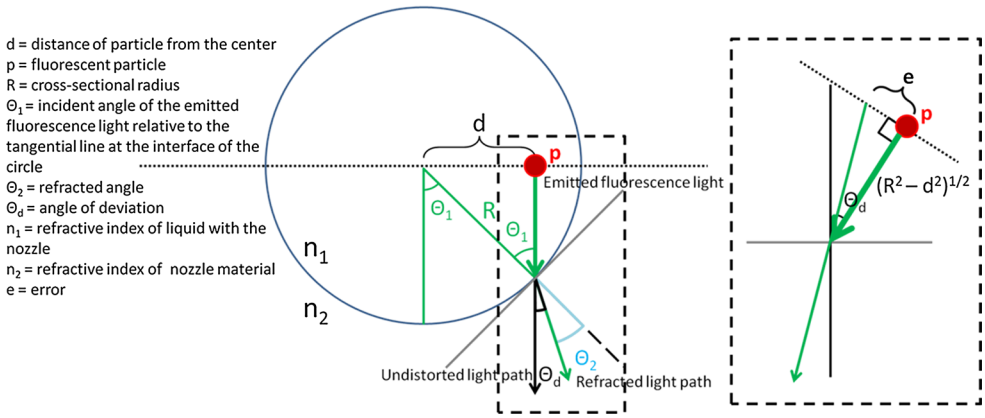

Fig. 10 Diagram depicting a cross section of the liquid–glass interface of the inkjet nozzle with a cross-sectional radius of R. Inset shows the emitted and refracted light path and the subsequent radial measurement error (e) which occurs

$$\theta_d = \theta_1 - \sin^{-1}\left(\frac{n_1 \cdot d}{n_2 \cdot r}\right) \tag{19}$$

$$\theta_d = \sin^{-1}\left(\frac{d}{r}\right) - \sin^{-1}\left(\frac{n_1 \cdot d}{n_2 \cdot r}\right) \tag{20}$$

Once θ_d was identified, the radial error (e) can be easily calculated from simple trigonometric identities as depicted by the inset in Fig. 10.

$$e = \sqrt{r^2 - d^2}\tan\left[\sin^{-1}\left(\frac{d}{R}\right) - \sin^{-1}\left(\frac{n_1 \cdot d}{n_2 \cdot R}\right)\right] \tag{21}$$

The radial error (e) and distance of the particle (d) can then be normalized by the total cross-sectional radius (R) to produce a profile of the expected radial error measurements along R. As expected, the error is zero during the case of $d = 0$ and $d = R$ with the error generally increasing with d.

References

Adrian RJ (1991) Particle-imaging techniques for experimental fluid mechanics. Annu Rev Fluid Mech 23:261–304

Alcock RD, Garner CP, Halliwell NA, Coupland JM (2004) An enhanced HPIV configuration for flow measurement through thick distorting windows. Meas Sci Technol 15:631

Boland T, Xu T, Damon B, Cui X (2006) Application of inkjet printing to tissue engineering. Biotechnol J 1:910–917

Bourdon CJ, Olsen MG, Gorby AD (2004) Power-filter technique for modifying depth of correlation in microPIV experiments. Exp Fluids 37:263–271

Castrejón-Pita JR, Hoath SD, Castrejón-Pita AA, Morrison NF, Hsiao W-K, Hutchings IM (2012a) Time-resolved particle image velocimetry within the nozzle of a drop-on-demand printhead. J Imaging Sci Technol 56:50401–1–50401–6

Castrejón-Pita JR, Hoath SD, Hutchings IM (2012b) Velocity profiles in a cylindrical liquid jet by reconstructed velocimetry. J Fluids Eng 134:011201

Chahal D, Ahmadi A, Cheung KC (2012) Improving piezoelectric cell printing accuracy and reliability through neutral buoyancy of suspensions. Biotechnol Bioeng 109:2932–2940

Chee M, Yang R, Hubbell E, Berno A, Huang XC, Stern D, Winkler J, Lockhart DJ, Morris MS, Fodor SP (1996) Accessing genetic information with high-density DNA arrays. Science 274:610–614

Cheng E, Ahmadi A, Cheung KC (2014) Investigation of the hydrodynamics of suspended cells for reliable inkjet cell printing. In: Proceedings of the ASME 2014 4th Joint US-European fluids engineering division summer meeting and 12th international conference on nanochannels, microchannels, and minichannels ICNMM2014-21583, pp V001T03A010; 8 p

Cole RW, Jinadasa T, Brown CM (2011) Measuring and interpreting point spread functions to determine confocal microscope resolution and ensure quality control. Nat Protoc 6:1929–1941

Cooley PW, Wallace DB, Antohe BV (2001) Applications of ink-jet printing technology to BioMEMS and microfluidic systems. SPIE conference on microfluidics and BioMEMS. In: vol. 4560. p 177–188

Derby B (2010) Inkjet printing of functional and structural materials: fluid property requirements, feature stability, and resolution. Annu Rev Mater Res 40:395–414

Dijksman JF (1984) Hydrodynamics of small tubular pumps. J Fluid Mech 139:173–191

Fakhfouri V, Mermoud G, Kim J, Martinoli A, Brugger J (2009) Drop-on-demand inkjet printing of SU-8 polymer. Micro Nanosyst 1:63–67

Kang KH, Lee SJ, Lee CM, Kang IS (2004) Quantitative visualization of flow inside an evaporating droplet using the ray tracing method. Meas Sci Technol 15:1104

Lemmo AV, Rose DJ, Tisone TC (1998) Inkjet dispensing technology: applications in drug discovery. Curr Opin Biotechnol 9:615–617

Lorber B, Hsiao W-K, Hutchings IM, Martin KR (2014) Adult rat retinal ganglion cells and glia can be printed by piezoelectric inkjet printing. Biofabrication 6:015001

Magdassi S (2009) The chemistry of inkjet inks. World scientific. pp 8

Mei J, Lovell MR, Mickle MH (2005) Formulation and processing of novel conductive solution inks in continuous inkjet printing of 3-D electric circuits. IEEE Trans Electron Packag Manuf 28:265–273

Meinhart CD, Zhang H (2000) The flow structure inside a microfabricated inkjet printhead. J Microelectromechanical Syst 9:67–75

Meinhart CD, Wereley ST, Gray MHB (2000) Volume illumination for two-dimensional particle image velocimetry. Meas Sci Technol 11:809

Minor G, Oshkai P, Djilali N (2007) Optical distortion correction for liquid droplet visualization using the ray tracing method: further considerations. Meas Sci Technol 18:L23

Mueller S, Llewellin EW, Mader HM (2010) The rheology of suspensions of solid particles. Proc R Soc Lond Math Phys Eng Sci 466:1201–1228

Nakamura M, Kobayashi A, Takagi F, Watanabe A, Hiruma Y, Ohuchi K, Iwasaki Y, Horie M, Morita I, Takatani S (2005) Biocompatible inkjet printing technique for designed seeding of individual living cells. Tissue Eng 11:1658–1666

Parker J, Merati P (1996) An investigation of turbulent Taylor-Couette flow using laser Doppler velocimetry in a refractive index matched facility. J Fluids Eng 118:810–818

Rossi M, Segura R, Cierpka C, Kähler CJ (2011) On the effect of particle image intensity and image preprocessing on the depth of correlation in micro-PIV. Exp Fluids 52:1063–1075

Sachs E, Cima M, Williams P, Brancazio D, Cornie J (1992) Three dimensional printing: rapid tooling and prototypes directly from a CAD model. J Manuf Sci Eng 114:481–488

Schoeppler M (2006) Diverging ink jet technologies and applications. NIP Digit Fabr Conf 2006:1–3

Shin D-Y, Smith PJ (2008) Theoretical investigation of the influence of nozzle diameter variation on the fabrication of thin film transistor liquid crystal display color filters. J Appl Phys 103:114905–114905–114905–114911

Shin D-Y, Grassia P, Derby B (2005) Oscillatory incompressible fluid flow in a tapered tube with a free surface in an inkjet print head. J Fluids Eng 127:98–109

Sirringhaus H, Kawase T, Friend RH, Shimoda T, Inbasekaran M, Wu W, Woo EP (2000) High-resolution inkjet printing of all-polymer transistor circuits. Science 290:2123–2126

Suh Y, Son G (2009) A sharp-interface level-set method for simulation of a piezoelectric inkjet process. Numer Heat Transf Part B Fundam 55:295–312

Wijshoff H (2004) Free surface flow and acousto-elastic interaction in piezo inkjet. Technical Proceedings of the 2004 NSTI nanotechnology conference and trade show In: vol. 2. p 215

Wijshoff H (2006) Manipulating drop formation in piezo acoustic inkjet. NIP Digit Fabr Conf 2006:79–82

Wijshoff H (2010) The dynamics of the piezo inkjet printhead operation. Phys Rep 491:77–177

Wormald SA, Coupland JM (2010) On measuring 3D flow within inkjet droplet streams using a digital holographic microscope. J Mod Opt 57:700–708

Xu Q, Basaran OA (2007) Computational analysis of drop-on-demand drop formation. Phys Fluids 1994-Present 19:102111

Xu C, Zhang M, Huang Y, Ogale A, Fu J, Markwald RR (2014) Study of droplet formation process during drop-on-demand inkjetting of living cell-laden bioink. Langmuir 30:9130–9138

Yang JC, Chien W, King M, Grosshandler WL (1997) A simple piezoelectric droplet generator. Exp Fluids 23:445–447

Yu J-D, Sakai S, Sethian JA (2007) Two-phase viscoelastic jetting. J Comput Phys 220:568–585